In-situ visualizing atomic structural evolution during crystallization in ternary Zr-Cu-Al bulk metallic glasses

Xiaoya Wei [1], Si Lan [1,2], Zhenduo Wu [1], Masato Ohnuma[3], Tamaki Shibayama[4], Seiichi Watanabe[4], Jie Zhou [5], Zhaoping Lu [5], Yang Ren [6], Xun-Li Wang [1,7*]

[1]Department of Physics and Materials Science, City University of Hong Kong, Hong Kong SAR

[2]Herbert Gleiter Institute of Nanoscience, Nanjing University of Science and Technology, 200 Xiaolingwei Avenue, Nanjing 210094, China

[3]Quantum Beam System Engineering, Faculty of Engineering, Hokkaido University, Japan

[4]Center for Advanced Research of Energy and Materials, Faculty of Engineering, Hokkaido University Japan

[5]State Key Laboratory for Advanced Metals and Materials, University of Science and Technology Beijing, P. R. China

[6]X-ray Science Divisions, Advance Photon Source, Argonne National Laboratory, USA

[7] City University of Hong Kong Shenzhen Research Institute, 8 Yuexing 1st Road, Shenzhen Hi-Tech Industrial Park, Shenzhen 518057, China

Abstract: A well-designed experimental method has been presented to in-situ visualize the amorphous-to-crystalline phase transformation of two glass formers at the atomic-length scale in the supercooled liquid region using a high voltage electron microscopy (HVEM). Analysis of the HVEM high-resolution images, supported by the in-situ synchrotron diffraction, further confirms previous observations of distinctively different crystallization pathways in the two Zr-Cu-Al alloys. Moreover, the HVEM results illustrate that isolated distributed nanocrystals with mutual orientation easily grew up from the $Zr_{56}Cu_{36}Al_8$, an average glass former, which follows a classical crystallization pathway; while density population poorly ordered atomic clusters with large misorientation suspended the growth in the $Zr_{46}Cu_{46}Al_8$, a good glass former, which might follow a unusual crystallization pathway. In addition, in-situ synchrotron diffraction measurements confirm that the $Zr_{56}Cu_{36}Al_8$ alloy finally crystallized into an extended structure, in contrast, the final crystalline product of $Zr_{46}Cu_{46}Al_8$ alloy possesses a damped structure. Our study provides a detailed microscopic understanding

of the crystallization behaviors in the supercooled liquids, showing that the density population nucleation site with large misorientation and the confined final crystalline structure contribute to the stability of Zr-Cu-Al supercooled liquids.

1. Introduction

Understanding the atomic rearrangement in the supercooled metallic glass-forming liquid could shed light on some basic properties, such as the phase stability, glass-forming ability and crystallization [1-3]. The technical difficulties of in-situ directly observing the atomic rearrangement process hinder the development of this kind of studies [4-6]. Most pioneer works were conducted by computer simulation or in the pseudo-atomic system such as micrometer scale colloidal particles [7-9]. The in-situ experimental observation of nucleation and growth process in the atomic resolution is still very challenging [10].

Since the high voltage electron microscopy has an ultra-high accelerating voltage, it possesses several unique advantages to studying the structure information of materials [11, 12]. The most attractive feature of HVEM is the high penetration power, which enables capturing clear microscopy images of relatively thick specimens. By contrast, specimens for conventional TEM, especially for the spherical aberration-corrected TEM (Cs-TEM), have to be prepared to very thin, which can only represent the thin-film structures instead of the structures of bulk samples [13]. With HVEM, a thicker specimen maintaining the bulk nature could be observed. In addition, the point-to-point resolution of HVEM could reach to 0.118 nm, which observes atomic-level resolution images for ‘bulk-like’ samples possible. Furthermore, the HVEM in the

Hokkaido University is equipped with a holder with a heating stage, which enables in-situ observation of microstructure evolution in the supercooled liquid region.

A previous study [4] found the unusual crystallization behavior in a good glass former, $Zr_{46}Cu_{46}Al_8$, which is characterized by site-saturated nucleation followed by slow growth and the conventional crystallization behavior in an average glass-former, $Zr_{56}Cu_{36}Al_8$. The details of the atomic, scale structure evolution mechanisms, i.e., how atoms rearrangement affect the crystallization kinetics, and how localized atomic orderings develop and finally form nanocrystals are less understood. Here in-situ HVEM was applied to directly visualizing the phase transformation from the disordered structure to ordered crystalline in the supercooled liquid region at the atomic scale. Time-resolved synchrotron diffraction experiments with pair distribution function analysis were conducted to corroborate the observation by HVEM.

2. Experiments

Amorphous alloys ingots with compositions of $Zr_{56}Cu_{36}Al_8$ and $Zr_{46}Cu_{46}Al_8$ (atomic %) were respectively prepared by arc melting from mixtures of Zr (99.99%), Cu (99.99%), Al (99.99%) in appropriate amounts under a Ti-gettered argon atmosphere. Each ingot was re-melted six times to ensure compositional homogeneity and quenched into cooper-mold with 3 mm diameter by suction casting under high purity Ar_2 atmosphere. Ion milling was used to prepare the thin foil specimens of alloys. In-situ TEM images were taken by JEM-ARM-1300 high voltage transmission electron microscope (HVEM) with accelerating voltage of 1250 kV at Hokkaido University. The samples were loaded on a holder with a heating stage during in-situ observation.

The auto-correlation function (ACF) was introduced into image analysis on the scale of 1-2 nm to determine the local ordering. The ACF is a method for obtaining a measure of the amount and extent of local ordering in TEM images [14]. This analysis can be used to quantitatively compare different and related samples. It has been used to characterize the degree of local ordering in various materials with amorphous, near amorphous or microcrystalline structures [15-17]. The HRTEM images were divided into 64 sub-images, each of which is corresponding to the small region with the dimension of 1.84 nm × 1.84 nm. ACF Image analysis was carried out using the software Digital Micrograph (Gatan, Inc.) and Image J.

The energy-dispersive X-ray spectroscopy (EDX) line scanning of a partially crystallized $Zr_{56}Cu_{36}Al_8$ sample was performed with Tecnai F20. The EDX elemental mapping of a partially crystallized $Zr_{46}Cu_{46}Al_8$ sample was performed with Titan G2 at Hokkaido University. The EDX results analysis was carried out using the Tecnai Imaging & Analysis (TIA).

In-situ synchrotron X-ray diffraction measurements were conducted at Beamline 11-ID-C of the Advanced Photon Source (APS), Argonne National Laboratory, using 114 keV X-rays. The samples were cut and polished to 1 mm, mounted on a sample holder in a Linkam heating stage. In-situ X-ray scattering data were collected using a Perkin Elmer detector with a time resolution of 1 second in the argon atmosphere. The structure factor S(Q), where Q is the momentum transfer, and the reduced pair distribution function G(r), where r is the correlation length, were deduced using software PDFgetx2 [18].

3. Results

Figure 1 shows the sample temperature profiles for the Zr56 sample (blue dots) and the Zr46 sample (red squares) during the in-situ HVEM experiments. To overcome the drifts caused by the heating process and the high-energy electron beam bombarding effect [5], the samples were slowly heated to the specific annealing temperatures step by step. The samples were held for a period (10 to 20 minutes) to be stabilized at the given annealing temperature and then the high-resolution images were continuously taken until next heating event. The supercooled liquid regions of two alloys were determined from the previous differential scanning calorimetry (DSC) profiles performed with a heating rate of 10 K/s [4]. The first annealing stage was chosen ~ 15 K below T_g, which was to prevent the overshot of beginning heating event. Then the annealing temperature was elevated to just above T_g. The third stage was ~15 K above T_g. For Zr56, the sample was further heated to ~ 35 K above T_g. For Zr46, since it has higher Tg (20 K higher than that of Zr56), we stopped at the third stage. The specific temperatures of annealing stages for two samples were listed in Table 1. The precision for temperature control was 1-2 K.

Previous studies on the phase stability of several kinds of metallic glasses under ultra-high-energy (2 MeV) electron beam irradiation indicated that the high-dose electron irradiation would accelerate the crystallization in the MGs with poor glass-forming ability (GFA) [19-21]. Although our incident electron energy was far less than 2 MeV and the phase stability of two BMG are good enough, slight structure damage was still unavoidable. Accordingly, in order to reduce the dose of the incident electron

beam and minimize the radiation damage, we enlarged the beam size and lowered the magnification during each heating process. Images were taken statistically from a specific area for each specimen beucause it is hard to avoid drifting in a high-resolution imaging filed. By applying this strategy, it is feasible to capture the crystallization process in the supercooled liquid state at the atomic scale using in-situ high-resolution TEM.

Figure 2 (a-d) display the high-resolution images of the Zr56 sample at the as-cast stage and different annealing stages. Figure 2 (e-h) are the images for the Zr46 sample at the as-cast stage and different annealing stages. At the as-cast state, both samples exhibit maze-like atomic arrangement with very few regions with short-range ordering as marked by squares in Figure 2 (a, e).

For the Zr56 sample annealed at 15 K below Tg, a few local lattice fringes limited in 1 nm began to appear in the amorphous matrix. With further increasing the temperature to 5 K above Tg, few nanocrystals around 2 nm dispersed in the Zr56 supercooled liquid, as shown in Figure 2 (b). After heating up to the third stage (15 K above Tg), we can see that numbers of nanocrystals formed and developed into a larger size with clear interfaces. Analysis of ACF-processed images, Figure 3 (a), revealed the nanocrystalline particles with mutual orientation. The average size of nanocrystals in this annealing stage is about 5 nm, as shown in Figure 2 (c). When reaching to the final state (35 K above Tg), the sample was crystallized with a very small fraction of amorphous matrix remaining at the end. Figure 4 (a) displays a high-angle annular dark-field (HAADF) image of a partially crystallized Zr56 sample. The presence of the

mass/thickness contrast suggests that its composition is non-uniform [22]. The bright regions, shown as a dendrite-liked structure with clear interfaces, represent the crystalline product, and the rest dark regions are the remaining amorphous matrix. Figure 4 (b) shows the EDX line profiles along the black line which is marked in Figure 4 (a). The line scan profiles indicate that the crystalline product is Zr-rich (~67% Zr) and Cu-poor (~33% Cu).

For the Zr46 sample, at the first annealing stage of 18K below Tg, it remained amorphous without any lattice fringes, which indicates good phase stability of Zr46 sample. When the second annealing stage (2 K above Tg) was reached, few atomic clusters no larger than 1 nm, as marked in Figure 2 (g), became visible. During the final annealing stage (12 K above Tg), local atomic clusters, with a high number density and small size, formed in the matrix. The atomic alignments in those clusters were not well developed at this stage. These clusters were poorly ordered and adjacent to each other, as shown in Figure 2 (h). From the ACF analysis results, as shown in Figure 3 (b), local patches of fringes also indicated that the current structure contained local ordering, furthermore, the orientation of those fringes also suggested the nanocrystalline particles were randomly oriented in the matrix. Poorly ordered atomic clusters describe these precipitates with tiny size, large local distortion of the atomic alignment, and random orientation corresponding with Figure 2 (h) and Figure 3 (b). Figure 5 (a) displays a HAADF image of a partially crystallized Zr46 sample. The crystalline product, shown as irregular shapes with messy boundaries, presents the bright contrast, and the remaining amorphous matrix presents the dark contrast. Figure 5 (b-d) show the EDX

mapping results of Figure 5 (a)'s region, which indicates that the crystalline product is Cu-rich.

Figures 6 (a) and (c) show the evolution of structure factor patterns, S(Q), as a function of annealing timefor the Zr56 and Zr46 samples at a same relative annealing temperature, respectively. Figures 6 (b) and (d) show that the corresponding G(r) patterns for the Zr56 and Zr46 samples, respectively. At the as-cast state, both S(Q) patterns displayed diffraction halos without Bragg peaks. Meantime, the G(r) profiles fall at large r due to the lack of long-range order, exhibiting typical features of fully amorphous materials.

For the Zr56 sample, the incubation period for crystallization is 150 min at 23 ± 1 K above its Tg, within which the diffraction patterns and pair distribution functions (PDFs) showed no discernable changes. Then, the intensity of diffraction peaks increased gradually at a steady rate, as shown in Figure 6 (a). After 4 hours annealing, the diffraction peaks became strong and sharp. The Rietveld refinement analysis shows that the final product of a fully crystallized Zr56 sample is the tetragonal Zr_2Cu, which is consistent with the EDX result shown in Figure 4. From Figure 6 (b), the PDF corresponding to 4 hours annealing extended to a high correlation length (beyond 30 Å), which indicates that the Zr_2Cu phase could quickly fill in space.

A Zr46 sample annealed 6 hours at 30 ± 1 K above its Tg, and the structural evolution was recorded as shown in Figure 6 (c-d) from 0 min to 360 min. Surprisingly, there is no signature of crystallization, which implies the strong stability against crystallization in the Zr46 supercooled liquid. The crystal pattern marked in Figure 6

(c, d) is the final crystallization state of Zr46 alloy, which was collected by annealing another sample at an elevated temperature, 55 ± 1 K above its Tg, for 30 min. The S(Q) pattern of crystallized state shows weak and broad diffraction peaks. According to the Rietveld refinement analysis of a fully crystallized Zr46 sample, the primary crystalline phase is orthorhombic $Cu_{10}Zr_7$. As shown in Figure 6 (d), the PDF of crystallized state damped fast, and strong pair correlation limited in 20 Å, which indicates that the $Cu_{10}Zr_7$ phase is a somewhat confined structure.

4. Discussions

The detailed atomic-scale information obtained from the in-situ HVEM demonstrates that the crystallization in the Zr56 alloy adequately follows continuous nucleation and growth, while that in the Zr46 alloy could not be so simply described, which is characterized by much longer induction time, site saturate nucleation and slower growth. Furthermore, HVEM results showed a significant discrepancy of nanocrystalline formation and initial crystal growth rate between two alloys. The mechanisms behind the crystallization of these two alloys under isothermal annealing in the supercooled liquid region could be different.

Classically, the crystallization precedes as following: nucleation clusters form during thermal fluctuation, and only the ones surpass a critical nucleation size could continue to grow to nuclei and grow into crystals, while those smaller than this critical size dissolve [23]. In the Zr56 supercooled liquid, the nuclei individually formed and separately distributed in the matrix, independently grew up into nanocrystals with 5-7 nm sizes, as shown in Figure 2 (a-c). Then the crystals of larger size were obtained,

which was indicated in Figure 2 (d) and HAADF image. On the other hand, from the synchrotron data, the crystal grows continuously during isothermal annealing. The final crystalline product is a highly-extended structure supported by the PDF results. All these evidence points to a possible outcome that the Zr56 alloy followed a classical nucleation and growth mechanism during isothermal annealing in the supercooled liquid region.

Recently, some *in-situ* observations and simulations revealed an unusual coarsening behavior in various systems and formulate a new mechanism of crystal growth, oriented attachment [24-27]. This particle-based non-classical crystallization can be divided into three main steps: 1. the formation of high density of 2-3 nm primary particles as the building blocks; 2. the spontaneous self-organization of adjacent particles with a common crystallographic orientation; 3. the aggregation of these particles at a planar interface, which allow the system to win the driving force by eliminating two high-energy surfaces, to form the final coarser polycrystalline products [28, 29]. Earlier, Lu et. al. [30, 31] demonstrated that poorly ordered clusters as precursors firstly formed and then shear-deposited at the crystal front in the Ni-P metallic glass system based on the in-situ TEM studies. In principle, there are two main possible ways achieved oriented attachment growth: one is an effective collision of particles with mutual orientation, another choice is coalescence by particle rotation to achieve a parallel orientation in infirmly solidified system where the particles possess rotation freedom [28]. For the Zr46 alloy, as shown in Figure 2 (e-h), saturated poorly ordered clusters around 2-3 nm appear adjacently with random orientation after a rather

long incubation time. These high density clusters consist well with the formation of the building blocks in the first step of particle based non-classical crystallization mechanisms. Then, they grew into polycrystalline with diffuse boundaries and confined size, indicated by the HAADF image, which may suggested the merge of these clusters in the matrix. Furthermore, the final fast damped structure suggested by the PDF results also supported a confined structure. Our results might suggest that the crystallization mechanism behind the Zr46 alloy is a particle-based non-classical oriented attachment. Since the time resolution for our experiment is limited, we missed some crystallization steps and are not sure how the particles rotated in the supercooled liquid matrix. However, to rotate and parallelize them required relatively high energy, which suspended the crystal growth in a certain extent. Further investigation with more advanced techniques should be conducted to study the physical insight of particles' random orientations and also the rotation process in the Zr46 supercooled liquid during crystallization.

5. Conclusions

To sum up, in-situ HVEM observation, supported by in-situ synchrotron diffraction illustrated the crystallization pathways in two Zr-based BMGs of different GFA at the atomic scale are different. Our experimental results reveled an unusual crystal growth mode for the Zr46 alloy of good GFA. By contrary to the classical crystallization pathway for Zr56 BMGs, an average glass former with an extended crystalline product, Zr46 BMGs, a better glass former with a damped crystalline product, would experience a more complex crystallization mechanism, so-called

oriented attachment, that is, the crystal growth suspended by the poorly ordered clusters with random orientation. This study also illustrated that the potential of HVEM as a tool to in-situ visualize the real-time structural evolution during the crystallization in BMGs at a atomic scale.

Acknowledgment

This work is supported by the Research Grants Council of Hong Kong Special Administrative Region (CityU Project No.11216215). X. L. Wang and SL acknowledge support by the National Natural Science Foundation of China (Grant No. 51571170, 51501090) and the Ministry of Science and Technology of China (Grant No. 2016YFA0401501). SL acknowledges the support by Natural Science Foundation of Jiangsu province with grant No. BK20171425. The use of the Advanced Photon Source, an Office of Science User Facility operated by the U.S. Department of Energy (DOE) by Argonne National Laboratory, was supported under DOE Contract No. DE-AC02-06CH11357.

References

[1] W.L. Johnson, Bulk Glass-Forming Metallic Alloys: Science and Technology, MRS Bulletin, **24** (1999), 42-56.
[2] D.B. Miracle, T. Egami, K.M. Flores, K.F. Kelton, Structural Aspects of Metallic Glasses, MRS Bulletin, **32** (2007), 629-634.
[3] Q. Wang, C.T. Liu, Y. Yang, Y.D. Dong, J. Lu, Atomic-Scale Structural Evolution and Stability of Supercooled Liquid of a Zr-Based Bulk Metallic Glass, Physical Review Letters, **106** (2011), 215505, 4.
[4] S. Lan, X. Wei, J. Zhou, Z. Lu, X. Wu, M. Feygenson, J. Neuefeind, X.-L. Wang, In-

situ study of crystallization kinetics in ternary bulk metallic glass alloys with different glass forming abilities, Applied physics letters, **105** (2014), 201906.
[5] X.J. Liu, G.L. Chen, H.Y. Hou, X. Hui, K.F. Yao, Z.P. Lu, C.T. Liu, Atomistic mechanism for nanocrystallization of metallic glasses, Acta Materialia, **56** (2008), 2760-2769.
[6] S. Lan, Z.D. Wu, M.T. Lau, H.W. Kui, Crystallization in homogeneous and phase-separated Pd41.25Ni41.25P17.5 bulk metallic glasses, Journal of Non-Crystalline Solids, **373** (2013), 5-12.
[7] P. Tan, N. Xu, L. Xu, Visualizing kinetic pathways of homogeneous nucleation in colloidal crystallization, Nature Physics, **10** (2014), 73-79.
[8] J. Russo, H. Tanaka, The microscopic pathway to crystallization in supercooled liquids, arXiv preprint arXiv:1109.0107, (2011).
[9] C.G. Tang, P. Harrowell, Anomalously slow crystal growth of the glass-forming alloy CuZr, Nature Materials, **12** (2013), 507-511.
[10] K.Q. Huang, C.R. Cao, Y.T. Sun, J. Li, H.Y. Bai, L. Gu, D.N. Zheng, W.H. Wang, Direct observation of atomic-level nucleation and growth processes from an ultrathin metallic glass films, Journal of Applied Physics, **119** (2016), 014305, 6.
[11] T. Shibayama, G. Matsuo, K. Hamada, S. Watanabe, H. Kishimoto, IOP Publishing, pp. 162013.
[12] S. Lan, Y. Ren, X.Y. Wei, B. Wang, E.P. Gilbert, T. Shibayama, S. Watanabe, M. Ohnuma, X.L. Wang, Hidden amorphous phase and reentrant supercooled liquid in Pd-Ni-P metallic glasses, Nature Communications, **8** (2017), 14679, 8.
[13] P. Zhang, J.J. Maldonis, Z. Liu, J. Schroers, P.M. Voyles, Spatially heterogeneous dynamics in a metallic glass forming liquid imaged by electron correlation microscopy, Nature Communications, **9** (2018), 1129.
[14] G.Y. Fan, J.M. Cowley, Auto-correlation analysis of high resolution electron micrographs of near-amorphous thin films, Ultramicroscopy, **17** (1985), 345-355.
[15] S.M. Chang, H.Y. Huang, H.Y. Yang, L.J. Chen, Mechanism of enhanced formation of C54-TiSi2 in high-temperature deposited Ti thin films on preamorphized (001) Si, Applied physics letters, **74** (1999), 224.
[16] L.J. Chen, S.L. Cheng, C.H. Yu, P.Y. Su, H.H. Lin, K.S. Chi, Structural evolution in amorphous silicon and germanium thin films, Microscopy and Microanalysis, **8** (2002), 268-273.
[17] Q. Wang, C.T. Liu, Y. Yang, J.B. Liu, Y.D. Dong, J. Lu, The atomic-scale mechanism for the enhanced glass-forming-ability of a Cu-Zr based bulk metallic glass with minor element additions, Scientific reports, **4** (2014).
[18] X. Qiu, J.W. Thompson, S.J.L. Billinge, PDFgetX2: a GUI-driven program to obtain the pair distribution function from X-ray powder diffraction data, Journal of Applied Crystallography, **37** (2004), 678-678.
[19] T. Nagase, T. Sanda, A. Nino, W. Qin, H. Yasuda, H. Mori, Y. Umakoshi, J.A. Szpunar, MeV electron irradiation induced crystallization in metallic glasses: Atomic structure, crystallization mechanism and stability of an amorphous phase under the irradiation, Journal of Non-Crystalline Solids, **358** (2012), 502-518.
[20] T. Nagase, Y. Umakoshi, Electron irradiation induced crystallization of the amorphous phase in Zr-Cu based metallic glasses with various thermal stability,

Materials Transactions, **45** (2004), 13-23.
[21] T. Nagase, Y. Umakoshi, N. Sumida, Formation of nanocrystalline structure during electron irradiation induced crystallization in amorphous Fe–Zr–B alloys, Science and Technology of Advanced Materials, **3** (2002), 119-128.
[22] S. Lan, Y.L. Yip, M.T. Lau, H.W. Kui, Direct imaging of phase separation in Pd41.25Ni41.25P17.5 bulk metallic glasses, Journal of Non-Crystalline Solids, **358** (2012), 1298-1302.
[23] K.F. Kelton, A.L. Greer, Nucleation in condensed matter: Applications in materials and biology, MA/Amsterdam: Elsevier/Pergamon, Boston, 2010.
[24] J.F. Banfield, S.A. Welch, H. Zhang, T.T. Ebert, R.L. Penn, Aggregation-Based Crystal Growth and Microstructure Development in Natural Iron Oxyhydroxide Biomineralization Products, Science, **289** (2000), 751-754.
[25] R.L. Penn, J.F. Banfield, Imperfect oriented attachment: Dislocation generation in defect-free nanocrystals, Science, **281** (1998), 969-971.
[26] D.S. Li, M.H. Nielsen, J.R.I. Lee, C. Frandsen, J.F. Banfield, J.J. De Yoreo, Direction-Specific Interactions Control Crystal Growth by Oriented Attachment, Science, **336** (2012), 1014-1018.
[27] J.M. Yuk, J. Park, P. Ercius, K. Kim, D.J. Hellebusch, M.F. Crommie, J.Y. Lee, A. Zettl, A.P. Alivisatos, High-Resolution EM of Colloidal Nanocrystal Growth Using Graphene Liquid Cells, Science, **336** (2012), 61-64.
[28] H. Cöelfen, M. Antonietti, Mesocrystals and nonclassical crystallization, John Wiley & Sons, 2008.
[29] Q. Zhang, S.-J. Liu, S.-H. Yu, Recent advances in oriented attachment growth and synthesis of functional materials: concept, evidence, mechanism, and future, Journal of Materials Chemistry, **19** (2009), 191-207.
[30] K. Lu, J.T. Wang, A new crystallization micromechanism for amorphous alloys, Materials Science and Engineering: A, **133** (1991), 504-508.
[31] K. Lu, J.T. Wang, CRYSTAL-GROWTH DURING CRYSTALLIZATION OF AMORPHOUS-ALLOYS, Journal of Crystal Growth, **94** (1989), 448-454.

Table 1: Temperature profiles for $Zr_{56}Cu_{36}Al_8$ (a) and $Zr_{46}Cu_{46}Al_8$ (b) samples.

		Stage 1	$T_{g\text{-}onset}$	Stage 2	Stage 3	Stage 4
$Zr_{56}Cu_{36}Al_8$	T (K)	653	668 [4]	673	683	703
	ΔT (K)*	-15	0	5	15	35
$Zr_{46}Cu_{46}Al_8$	T (K)	673	691 [4]	693	703	
	ΔT (K)*	-18	0	2	12	

*: $\Delta T=T-T_{g\text{-}onset}$.

Captions

Figure 1. Temperature profiles for $Zr_{56}Cu_{36}Al_8$ and $Zr_{46}Cu_{46}Al_8$ samples.

Figure 2. The HRTEM images for $Zr_{56}Cu_{36}Al_8$ (a) and $Zr_{56}Cu_{36}Al_8$ (a) in as-cast state, which show random atomic arrangement with very few short-range ordering regions as marked by red and yellow squares for $Zr_{56}Cu_{36}Al_8$ and $Zr_{46}Cu_{46}Al_8$, respectively. (b-d) and (f-h) are the HRTEM images for $Zr_{56}Cu_{36}Al_8$ and $Zr_{46}Cu_{46}Al_8$ isothermal annealed for different time, respectively. The nanocrystals formed in the $Zr_{56}Cu_{36}Al_8$ matrix have been marked by red spheres, and poorly ordered clusters formed in the $Zr_{46}Cu_{46}Al_8$ have been marked by yellow squares.

Figure 3. The ACF-processed 1.84 nm × 1.84 nm images corresponding to Figure 2 (c) for $Zr_{56}Cu_{36}Al_8$ (a) and corresponding to Figure 2 (h) for $Zr_{46}Cu_{46}Al_8$ (b), respectively.

Figure 4. The HADDF image (a) and EDX line scan profiles (b) along the black line

marked in the (a) for the partially crystalline state of $Zr_{56}Cu_{36}Al_8$.

Figure 5. The HADDF image (a) and EDX element mapping for Zr, Cu and Al (b-d) for the partially crystalline state of $Zr_{46}Cu_{46}Al_8$.

Figure 6. The S(Q) (a) and PDF (b) evolution during isothermal annealing for $Zr_{56}Cu_{36}Al_8$. The structure evolution during isothermal annealing at 30 ± 1K lasting 360 min and also the structure information of the final crystalline product noted as Cryst. which is obtained at 55 ± 1 K lasting 30 min for $Zr_{46}Cu_{46}Al_8$ are shown as S(Q) (c) and PDF (d) patterns.

Figure 1.

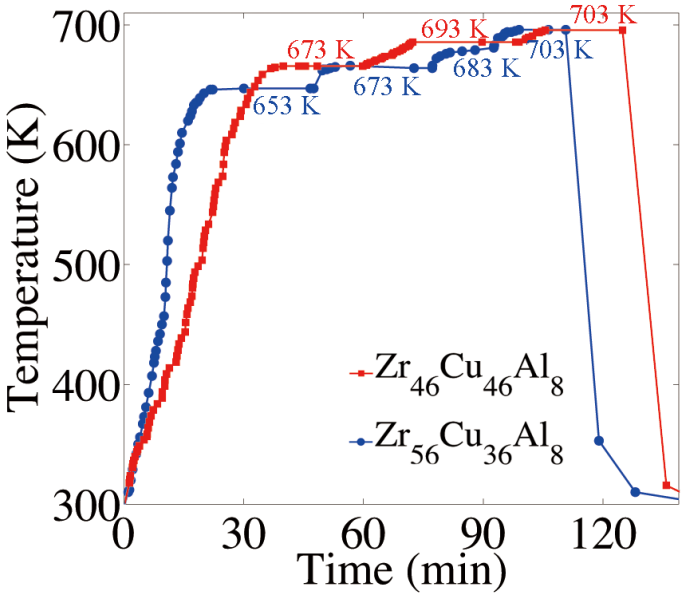

Figure 2.

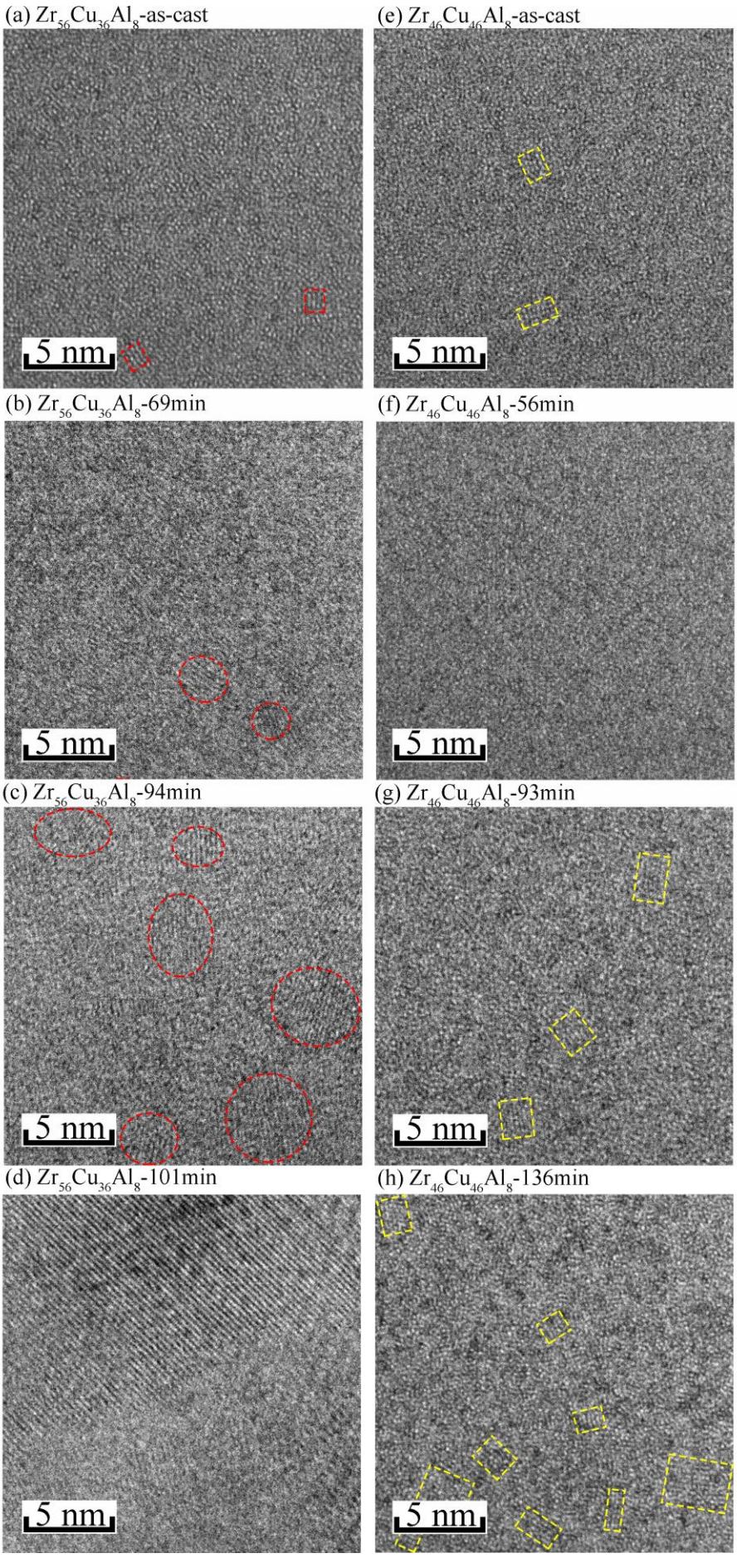
(a) $Zr_{56}Cu_{36}Al_8$-as-cast
(e) $Zr_{46}Cu_{46}Al_8$-as-cast
(b) $Zr_{56}Cu_{36}Al_8$-69min
(f) $Zr_{46}Cu_{46}Al_8$-56min
(c) $Zr_{56}Cu_{36}Al_8$-94min
(g) $Zr_{46}Cu_{46}Al_8$-93min
(d) $Zr_{56}Cu_{36}Al_8$-101min
(h) $Zr_{46}Cu_{46}Al_8$-136min
5 nm

Figure 3.

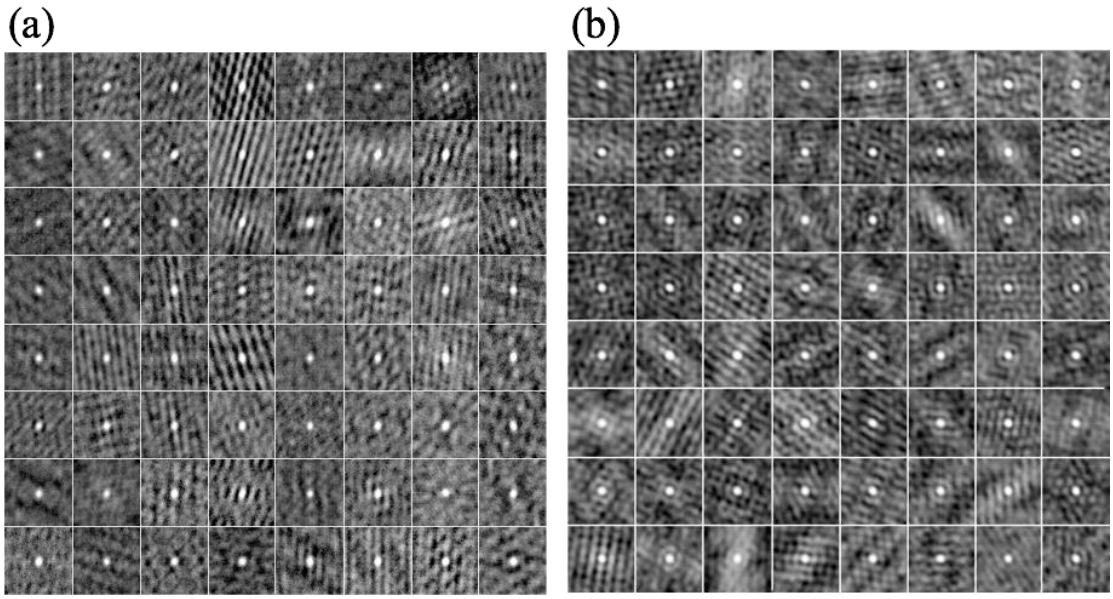

Figure 4.

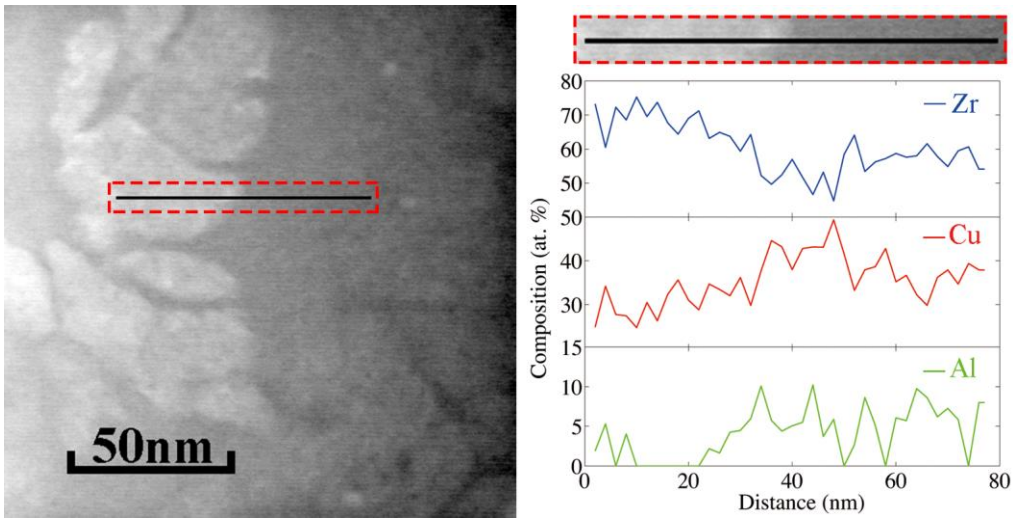

Figure 5.

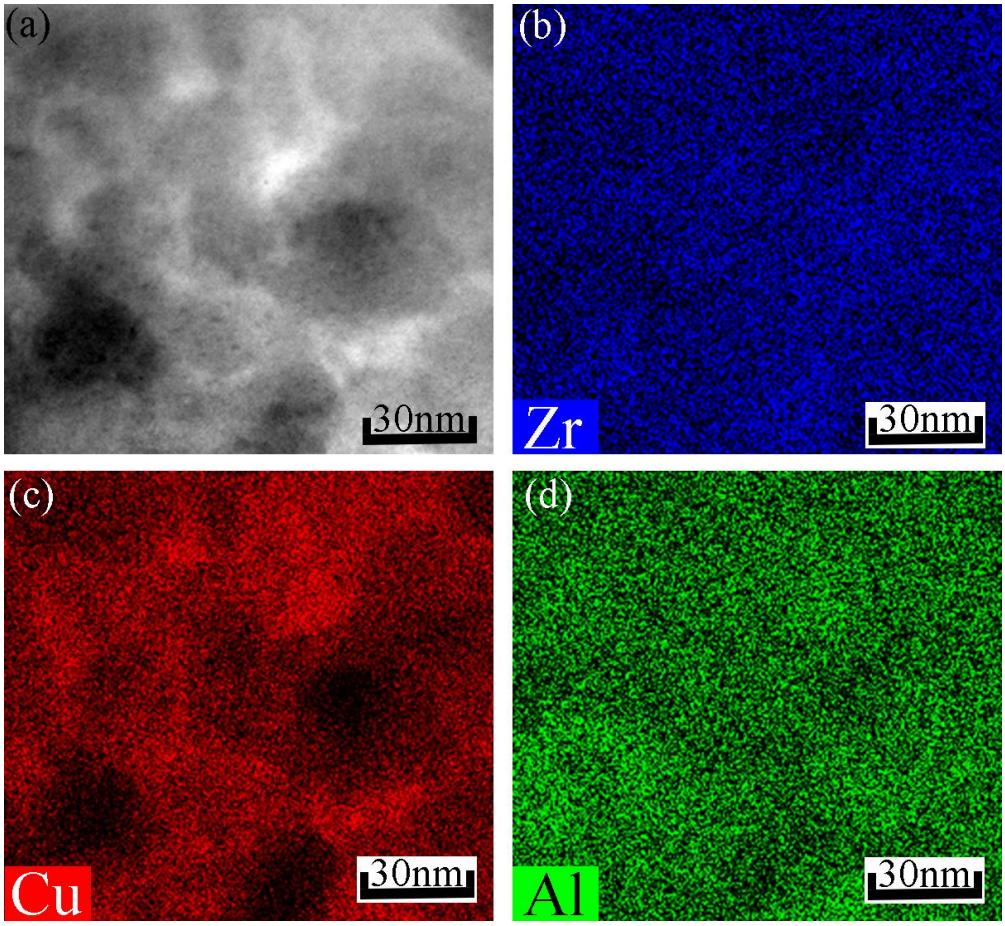

Figure 6.

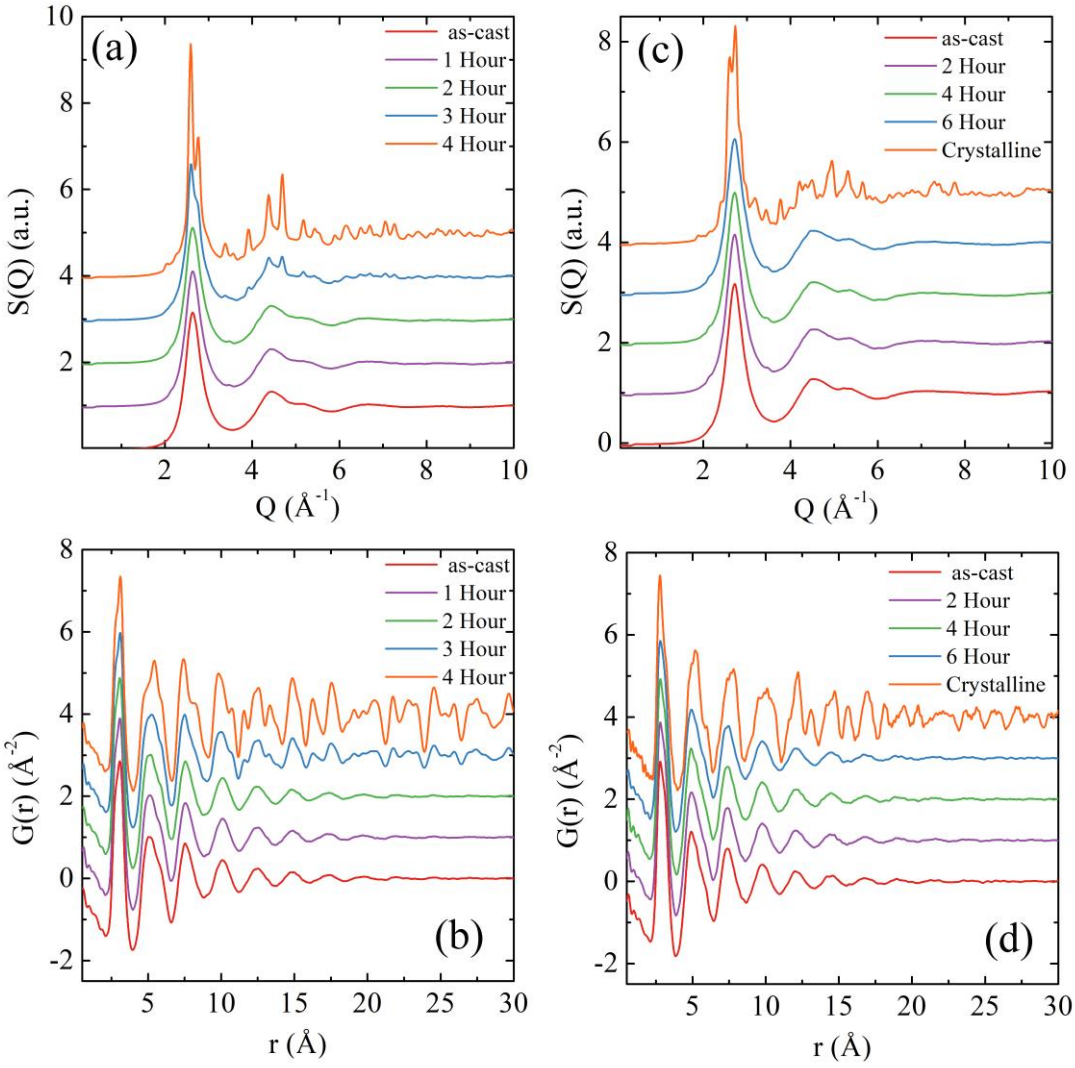
(a)
as-cast
1 Hour
2 Hour
3 Hour
4 Hour
S(Q) (a.u.)
Q (Å^{-1})
(c)
as-cast
2 Hour
4 Hour
6 Hour
Crystalline
S(Q) (a.u.)
Q (Å^{-1})
(b)
as-cast
1 Hour
2 Hour
3 Hour
4 Hour
G(r) (Å^{-2})
r (Å)
(d)
as-cast
2 Hour
4 Hour
6 Hour
Crystalline
G(r) (Å^{-2})
r (Å)